Oblique transition in a laminar Blasius boundary layer

By RUDOLPH A. KING[1] AND KENNETH S. BREUER[2]

[1]NASA Langley Research Center, Hampton, VA 23681, USA
[2]Division of Engineering, Brown University, Providence, RI 02912, USA

Oblique transition was experimentally investigated in a Blasius boundary layer formed on a flat plate. This transition mechanism was provoked by exciting a pair of oppositely oriented oblique Orr–Sommerfeld (O–S) modes given by $(\omega/\omega_{ts}, \pm\beta/\beta_{ts}) = (1, \pm1)$ in the frequency–wavenumber (spanwise) space. Surface waviness with height Δh and a well-defined wavenumber spectrum that is synchronized with the neutral O–S wavenumber at Branch I, $(\alpha_w, \pm\beta_w) = (\alpha_{ts,I}, \pm\beta_{ts,I})$, was used to provide a steady velocity perturbation in the near-wall region. A planar downstream-travelling acoustic wave of amplitude ϵ was created to temporally excite the flow near the resonance frequency, $\omega_{ts}(= 2\pi f_o)$, of an unstable eigenmode corresponding to $k_{ts} = k_w$ (where $k = \pm[\alpha^2 + \beta^2]^{1/2}$). Possible mechanisms leading to laminar-to-turbulent breakdown were examined for various forcing combinations, $\epsilon\Delta h$. For small values of $\epsilon\Delta h$, a peak–valley structure corresponding to a spanwise wavenumber of $2\beta_w$ was observed. As expected, the maximum r.m.s. narrow-band streamwise velocity fluctuations, $u_t(f_o)$, occur at peak locations, which correspond to regions with mean streamwise velocity, U, deficits. For the largest value of $\epsilon\Delta h$, significant mean-flow distortion was observed in the spanwise profiles of U. Large spanwise velocity gradients, $|dU/d\zeta|$, exist between peaks and valleys and appear to generate an explosive growth in the velocity fluctuations. The maximum values of u_t no longer occur at peak locations of the stationary structure but at locations of spanwise inflection points. The magnitude of u_t scales with $|dU/d\zeta|$. A nonlinear interaction of two non-stationary modes was conjectured as a possible mechanism for the enhancement of the streak amplification rate.

1. Introduction

Many important gaps remain in our understanding of laminar-to-turbulent transition in fluid mechanics. The state of a boundary layer, laminar or turbulent, dramatically affects parameters such as skin friction, form drag, heat transfer rates, etc. Practical applications that are affected include, but are not limited to, controllability of airfoils and high-lift devices, turbine and engine performance, and aircraft and spacecraft performance. A fundamental understanding of the laminar-to-turbulent transition process can lead to improved transition prediction techniques and eventually transition control methodologies.

It has long been recognized that the occurrence of three-dimensional disturbances (secondary instability) is necessary for the laminar-to-turbulent transition process (see for example Klebanoff & Tidstrom 1959; Klebanoff, Tidstrom & Sargent 1962). The breakdown scenario observed by Klebanoff *et al.* is referred to as fundamental or

K-type breakdown and begins with the amplification of initially two-dimensional Tollmien–Schlichting (T–S) waves. As these primary T–S waves exceed a threshold value of typically 1% of the free-stream velocity, three-dimensional structures evolve with spanwise periodicity of alternating *peaks* and *valleys* and result in an aligned peak–valley structure. Using Floquet theory of secondary instability, Herbert (1985) showed that for large initial two-dimensional T–S amplitudes relative to random background disturbances, primary resonance occurs leading to K-type breakdown. A different route to transition, subharmonic breakdown, was first observed Knapp & Roache (1968) on an ogive cylinder and was characterized by a staggered peak–valley structure. Self-excited (three-dimensional excitation derived from the background disturbance environment) and/or controlled subharmonic spectral energy have been experimentally observed on flat-plate boundary layers (e.g. Kachanov, Kozlov & Levchenko 1977; Saric, Kozlov & Levchenko 1984; Saric & Thomas 1984; Kachanov & Levchenko 1984; Corke & Mangano 1989). Subharmonic breakdown is characterized by small two-dimensional T–S amplitudes (typically less than 0.3% of the free-stream velocity) and produce either a C-type (see Craik 1971) or H-type (see Herbert 1988) breakdown, where H-type is the more general type of subharmonic instability that occurs for a broad band of spanwise wavenumbers as a result of parametric resonance.

The evolution of wavepackets (see Gaster & Grant 1975) in laminar boundary layers has also been studied as a model of *natural* transition to turbulence since a wavepacket produces a broad spectrum of frequencies and spanwise wavenumbers. The evolution of a localized disturbance in a laminar boundary layer from a low-amplitude wavepacket to the formation of a turbulent spot has been experimentally studied by Cohen, Breuer & Haritonidis (1991) and Breuer, Cohen & Haritonidis (1997). In the linear stage of the wavepacket evolution, the wavenumber–frequency spectra indicated that most of the energy was concentrated in two-dimensional modes centred about a fundamental frequency corresponding to the most-amplified mode according to linear stability theory (LST). As nonlinear effects evolve in the wavepacket, increased energy corresponding to oblique modes at a frequency one-half of the fundamental (subharmonic modes) were observed to be dominant in the wavenumber–frequency spectra. The spanwise wavenumber corresponding to these oblique modes suggested that the modes grew as a subharmonic resonance triad as described by Craik (1971).

The transition scenarios discussed above all start with strong two-dimensional modes, but as the three-dimensional modes gain energy, transition advances rapidly. The selection process of boundary layers has identified oblique modes as an essential ingredient for the onset of laminar-to-turbulent breakdown. Recognizing that direct seeding of oblique modes may be very efficient as a transition promoter, Schmid & Henningson (1992), using direct numerical simulations (temporal) applied to a channel flow, investigated a transition mechanism involving a pair of oblique O–S modes $(f, \pm\beta)$ in the frequency/spanwise-wavenumber space, the so-called *oblique* transition. They found that this transition scenario occurred at a much faster time scale than the one for secondary instability, assuming the same input disturbance energy for both scenarios. They also found that nonlinear interactions were mainly responsible for the initial energy transfer to other spanwise modes that then grew by linear mechanisms. The dominance of the linear transfer mechanism was reduced as transition was approached. Later, Joslin, Streett & Chang (1993) and Berlin, Lundbladh & Henningson (1994) applied spatial numerical simulations covering the transition process to a Blasius boundary layer. This transition scenario was conjectured as a

three stage process: (i) a nonlinear interaction of the primary disturbances $(f, \pm\beta)$ to generate a streamwise vortex system $(0, 2\beta)$, (ii) a transient growth region of low- and high-speed streaks produced by the vortex system, and (iii) ultimate breakdown of the streaks instigated by non-stationary disturbances due to secondary instability. Subcritical transition resulting from transient disturbance growth was found to be possible, thereby *bypassing* (see Morkovin 1969) the exponential amplification of T–S instabilities.

Elofsson & Alfredsson (1998, 2000) and Wiegel (1996) verified oblique transition in physical experiments. The experiment by Elofsson & Alfredsson (1998) was conducted in a plane Poiseuille flow air channel in which oblique waves were generated by two vibrating ribbons, one on each wall. Wiegel's (1996) and Elofsson & Alfredsson's (2000) experimental investigations were conducted in zero-pressure-gradient boundary layers where controlled disturbances in the form of periodic blowing/suction were introduced through surface slots. Other experiments have been conducted to study the algebraic growth (see Landahl 1980 for discussion on algebraic instabilities) of the streaky structures and ultimate breakdown of the flow by direct generation of streaks. The origin of the streaks is not so important since all of these mechanisms generate streaks, some more efficiently than others depending on the initial conditions. Once the streaks are established, the mechanisms thereafter are the same. Elofsson, Kawakami & Alfredsson (1999) experimentally studied in a plane Poiseuille flow the development and stability of streamwise streaks generated by continuous suction through small wall slots. They found that if the streak amplitude exceeded a threshold value, secondary instability ensued in the form of travelling waves that give rise to high r.m.s. (root-mean-square) fluctuating velocities in the region of large spanwise mean-flow gradients. Similar findings were obtained by Bakchinov *et al.* (1995) in a flat-plate boundary layer modulated by stationary streamwise vortices generated by means of roughness elements arranged in a regular spanwise array. Wiegel & Fischer (1995) used non-intrusive optical techniques to study the structure of a Blasius boundary layer undergoing transition. They utilized controlled input disturbances in the form of periodic pressure oscillations through surface slots to control initial amplitudes of possible two-dimensional and oblique disturbances. By adjusting the relative amplitudes of the disturbances, they were able to visualize the following transition types: fundamental (K-type), subharmonic (C-type and H-type), and oblique type transition. For the oblique transition scenario, streamwise streaky structures with small α were observed that ultimately resulted in breakdown to turbulence – see also Berlin, Wiegel & Henningson (1999).

The primary objectives of this research were to provide careful experiments that can identify the controlling physics of the laminar-to-turbulent transition process, in particular oblique transition, and to supply a potential database for comparison with theory and/or numerical simulations. This study is a logical extension of the work by King & Breuer (2001) where two-dimensional and oblique T–S disturbances were introduced into a Blasius boundary layer via a non-localized receptivity mechanism. The earlier work demonstrated the use of a planar downstream-travelling acoustic wave and well-defined receptivity sites to produce a variety of T–S boundary-layer instability waves. A similar receptivity mechanism was utilized in the current study to excite the desired boundary-layer disturbance modes. Because of the particularly *clean* method used for the generation of the pair of oppositely oriented oblique modes via acoustic–roughness interactions, the approach provides a framework for making accurate measurements, and to the authors' knowledge such measurements have not been made in boundary-layer flows. The time scales and the spatial scales

are completely decoupled – the former being provided by the acoustic field and the latter coming from the surface roughness pattern. Experimental documentation of the subsequent development of the broadband boundary-layer disturbance evolution for various forcing combinations ($\epsilon \Delta h$) was acquired. The modal velocities, i.e. for a given frequency and spanwise wavenumber, were mapped along the streamwise direction for the primary (or initially excited) modes and higher-order modes resulting from nonlinear interactions. The experimental results were compared qualitatively and quantitatively, when possible, with theoretical and numerical simulation results when available.

2. Experimental details

2.1. *Facility and model*

The experimental setup of the current study is essentially the same as used by King & Breuer (2001) for the high-precision receptivity measurements. A brief description is given here for completeness. The study was conducted in the 2 ft (60.96 cm) by 3 ft (91.44 cm) Low-Speed Wind Tunnel located at NASA Langley Research Center. The maximum attainable speed in this closed-loop tunnel is approximately $45 \, \mathrm{m \, s^{-1}}$ with measured turbulence intensities, u/U_∞, of approximately 0.1% in the range of $0.1 < f < 400 \, \mathrm{Hz}$. Two motorized traverse stages, one with streamwise travel of 2.1 m and the other with vertical travel of 150 mm, are located just above the test section ceiling. A 3.8 cm streamwise slot (covered with rectangular wool felt strips to minimize air inflow/outflow) along the centreline of the tunnel ceiling is provided to accommodate support for a third traverse motion. This third spanwise (z) traverse component with a travel of 11.43 cm was installed in the tunnel test section. Streamlined cross-sections of the stage support and probe holder support were selected to minimize flow interference (maximum thickness-to-chord ratios are 16% and 15%, respectively). The quoted accuracy of the spanwise component is $\pm 125 \, \mathrm{\mu m \, m^{-1}}$.

The model tested was a 12.7 mm thick flat aluminium jig plate with a 24:1 elliptical leading edge (see figure 1). The highly polished (0.2 μm r.m.s. surface finish) plate was equipped with a rectangular hole located 24.6 cm from the model leading edge for the installation/removal of plate inserts. One plate insert was used as the baseline (smooth sample) and three were used to mount the receptivity sites.

2.2. *Surface roughness and acoustic excitation*

Oppositely oriented oblique O–S modes were introduced into the boundary layer using surface roughness of height Δh and free-stream acoustic excitation with amplitude u_{ac} as done by King & Breuer (2001) for two-dimensional and oblique modes. The roughness patterns were generated by applying a photolithographic process to copper-plated circuit boards. The pattern considered is represented in figure 2 (the shaded areas represent copper and flow is from top to bottom). The pattern consisted of two oppositely oriented oblique waves with $\psi_w = \pm 30°$. Highly localized disturbances are possible as a result of the sharp steps formed by the copper strips at the leading and trailing edges of the samples. To mitigate this effect, the copper strips were feathered down to the substrate material 6.4 mm from both the leading and trailing edges of the samples. Different roughness heights were considered by using three types of boards with different copper plating thicknesses. The roughness patterns considered in this study are presented in table 1.

The tunnel was equipped with an array of five 203.3 mm diameter woofers (four

Sample	Δh(μm)	$\lambda_{w,x}$ (mm)	ψ_w(deg.)
1	17.8	52.36	± 30
2	35.6	52.36	± 30
3	71.1	52.36	± 30

TABLE 1. Roughness samples tested, where $\lambda_{w,x}$ is the streamwise wavelength.
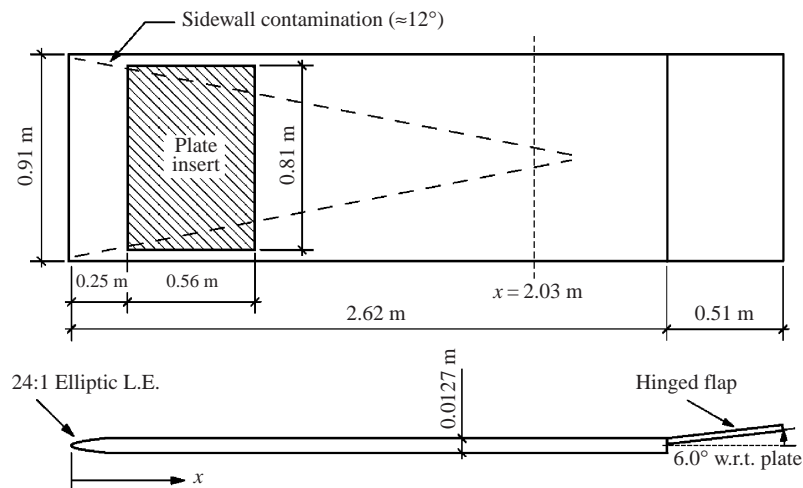

FIGURE 1. Top and side views of flat plate model. The shaded region represents the location of the insert. Vertical distances not to scale.
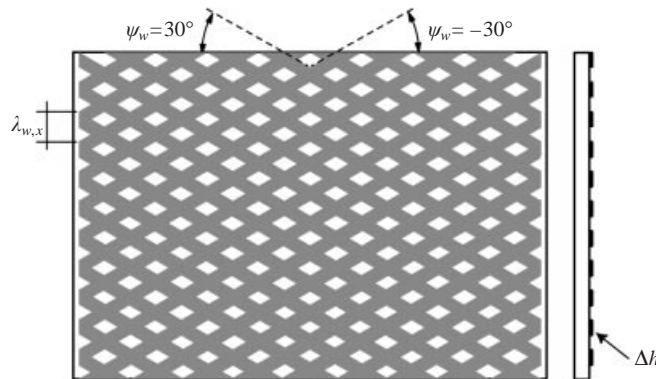

FIGURE 2. Top and side views of receptivity site investigated for $\psi_w = \pm 30°$. Flow is from top to bottom.

flush mounted on the upstream wall and the other on the downstream wall) for acoustic excitation. The source of the controlled acoustic field was generated by using a dual-channel universal source and amplified with a stereo power amplifier – one channel for the upstream speakers and the second channel for the downstream speaker. The ability to control the absolute amplitude and relative phase of the two channels made it possible to generate the required acoustic field in the test section.

2.3. *Data reduction*

Most of the experimental data, streamwise velocity component, were measured using a single-element hot-wire probe with a constant-temperature anemometer system. Broadband and phase-locked velocity fluctuations were acquired using a typical sampling rate of 1 kHz. The mean tunnel properties (pressures, temperature and relative humidity) were measured and recorded at each data point. Estimated uncertainties of measured mean velocity, U, are in the range $\pm 1.4\%$ for $U_{max} \approx 11.1\,\mathrm{m\,s^{-1}}$ to $\pm 9.0\%$ for $U_{min} \approx 1\,\mathrm{m\,s^{-1}}$. Uncertainties of r.m.s. fluctuating velocity, u, and Reynolds number, Re_l ($= U_\infty l/v$), are $\pm 4.7\%$ and $\pm 4.0\%$, respectively. Details of the error analysis are given by King (2000, Appendix A).

Because of the type of acoustic excitation (i.e. continuous wave), the measured r.m.s. narrow-band velocities $u_t \exp(\mathrm{i}\phi_t)$ – amplitude u_t and phase ϕ_t – included the Stokes wave (present whenever an oscillating velocity disturbance exists in the free stream), the T–S response, and any other extraneous response (e.g. probe vibration) all at the same excitation frequency f_o. The methods utilized to decompose the T–S wave from the measured disturbance are those discussed by King & Breuer (2001). One decomposition approach is to make short streamwise surveys that cover approximately one T–S wavelength, λ_{ts}, at a fixed height in the boundary layer. Over one λ_{ts}, the phase of the Stokes wave (and for that matter any probe vibration) is for all practical purposes constant. Since the T–S amplitude does not vary significantly over one λ_{ts}, the centroids (Stokes wave + vibration) and the average radii (T–S amplitudes) of the off-centred spirals, when plotted on the polar complex plane, can be computed. The second decomposition approach used here to extract the T–S wave component utilized two sets of wall-normal disturbance profiles at the same x-locations and with the same acoustic forcing levels. One set was taken with the smooth surface (including the Stokes wave, T–S wave due to leading-edge receptivity, and extraneous disturbances), and the other with the surface roughness (including the same components as smooth surface plus the T–S wave due to roughness). The T–S wave due to roughness was obtained by subtracting in the complex plane the smooth surface profiles from the rough surface profiles. As discussed by King & Breuer (2001), the T–S component here includes receptivity due to acoustic scattering at the roughness sites of (i) the free-stream acoustic field and (ii) the leading-edge generated T–S wave. The roughness receptivity due to the scattering of the leading-edge generated T–S wave at the roughness sites was negligibly small compared to that due to the free-stream acoustic field.

2.4. *Experimental approach*

The experiment was conducted with a nominal free-stream velocity of $U_\infty = 11.1\,\mathrm{m\,s^{-1}}$ and temperature of 21 °C. A nominally zero-streamwise-pressure-gradient boundary layer was obtained for flow over a flat plate (Blasius flow). A planar downstream-travelling acoustic wave was used to temporally excite the flow with frequency $f_o = 71\,\mathrm{Hz}$ in the same manner as done by King & Breuer (2001). This translates to a dimensionless frequency for the excited oblique O–S modes of $F = 55 \times 10^{-6}$ ($= 2\pi f v/U_\infty^2$). The streamwise spatial extent of the three-dimensional surface roughness was $\Delta x = 0.56\,\mathrm{m}$. The location of the surface roughness was selected such that its midpoint was near the location of Branch I ($R_I = 578$) for the primary oblique waves, to enhance the receptivity process. The wavenumber of the surface roughness k_w was selected such that it matched the neutral O–S wavenumber k_{ts} at Branch I, i.e. $(\alpha_w, \pm\beta_w) = (\alpha_{ts,I}, \pm\beta_{ts,I})$, to provide a near-resonance condition. Three roughness heights, Δh, and three acoustic forcing levels, ϵ ($= u_{ac}/U_\infty$), were examined resulting

	Δh_1	$\Delta h_2 = 2\Delta h_1$	$\Delta h_3 = 4\Delta h_1$
ϵ_1	$\epsilon_1\Delta h_1$	$2\epsilon_1\Delta h_1$	$4\epsilon_1\Delta h_1$
$\epsilon_2 \doteq 2\epsilon_1$	$2\epsilon_1\Delta h_1$	$4\epsilon_1\Delta h_1$	$8\epsilon_1\Delta h_1$
$\epsilon_3 \doteq 4\epsilon_1$	$4\epsilon_1\Delta h_1$	$8\epsilon_1\Delta h_1$	$16\epsilon_1\Delta h_1$

TABLE 2. Roughness heights and forcing levels examined; $\Delta h_1 = 17.8\,\mu\text{m}$, $\epsilon_1 = 7.6 \times 10^{-5}$ ($SPL = 84.8$).
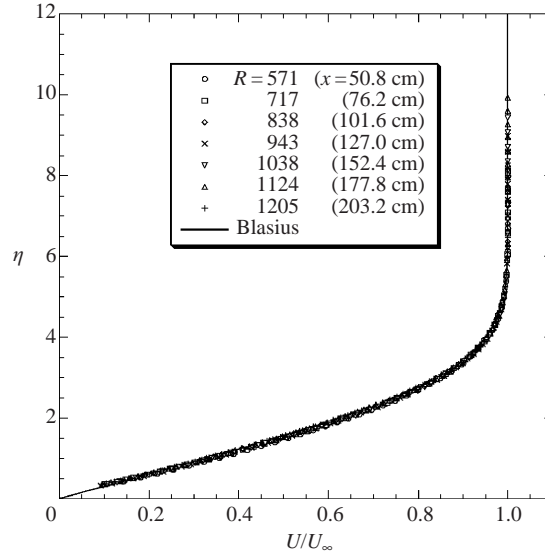
FIGURE 3. Normalized velocity profiles at selected streamwise locations along the tunnel centreline.

in a matrix configuration as depicted in table 2. The smallest Δh and ϵ examined are $\Delta h_1 = 17.8\,\mu\text{m}$ and $\epsilon_1 = 7.6 \times 10^{-5}$ (i.e. $SPL = 84.8$).

3. Results and discussion

3.1. *Base flow measurements*

The base flow in this study is the same as that used by King & Breuer (2001) to acquire the two-dimensional and oblique receptivity measurements. A synopsis of those results is presented here. The values of the experimental shape factors were $H = 2.60 \pm 1.5\%$, in excellent agreement with the theoretical Blasius value of $H = 2.59$. A plot of the measured normalized velocity profiles (along the tunnel centreline) and the theoretical Blasius profile versus the normalized wall-normal coordinate η ($= [y/x_v]Re_{x_v}^{1/2}$) is presented in figure 3. Note that x_v is the streamwise distance measured relative to the experimentally acquired virtual origin, $x = 65.8\,\text{mm}$. Free-stream turbulent intensities of $(u/U)_\infty \approx 0.1\%$ ($0.1 < f < 400\,\text{Hz}$) were measured over the entire streamwise survey region. Measured free-stream PSDs of $(u/U)_\infty$ indicate decaying spectra with the dominant energy contained within $0.1 < f < 1\,\text{Hz}$ (see the typical plot in figure 4). Some unavoidable electronic noise is observed in the spectrum due in part to extremely low signal levels. Correlations between signals obtained from wall-mounted dynamic pressure sensors (four) confirm the absence
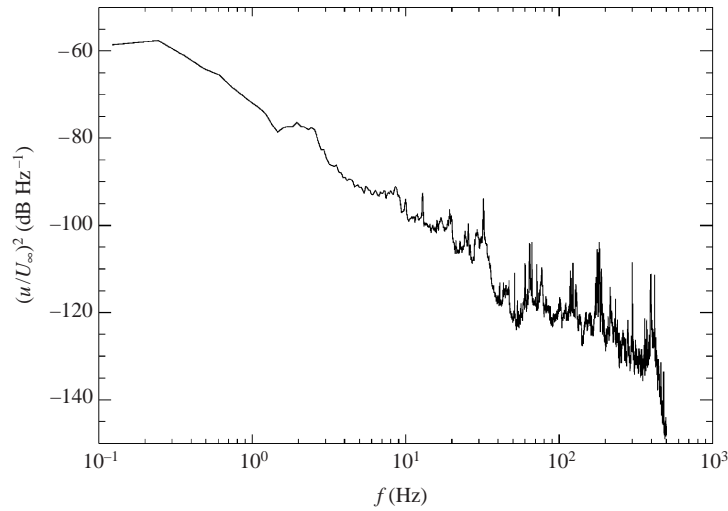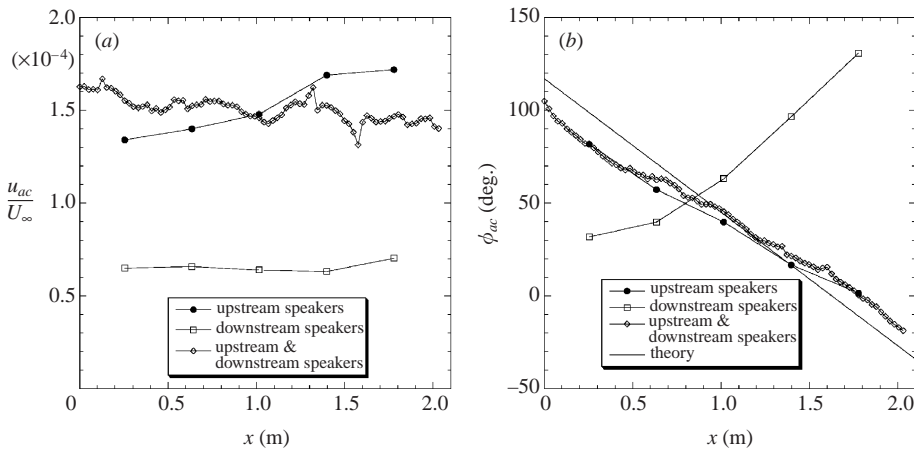
FIGURE 4. Free-stream velocity spectra at $x = 25.4$ cm, $y = 2.54$ cm, and $z = 0$.

FIGURE 5. Measured free-stream acoustic field generated in the test section above the model surface: (*a*) amplitude and (*b*) phase streamwise distributions.

of coherent disturbances in the free-stream environment near the designed forcing frequency, f_o, of the experiment that can possibly distort the interpretation of the results (details given by King 2000, his Appendix B).

Measurements of the controlled free-stream acoustic field are shown in figure 5 in the form of (*a*) amplitude and (*b*) phase streamwise distributions. Data with only the upstream speakers and only the downstream speaker activated are also presented for completeness in the figure. The phase distribution in part (*b*) of the figure indicates a predominantly downstream-travelling wave. Values of the acoustic r.m.s. amplitude, u_{ac}, used for normalization in subsequent sections are the average values measured over the plate insert.

3.2. *Peak–valley structure of the disturbance field*

A detailed view of the three-dimensional surface roughness pattern (recall figure 2) along with a coordinate description is shown in figure 6. The free-stream flow is in
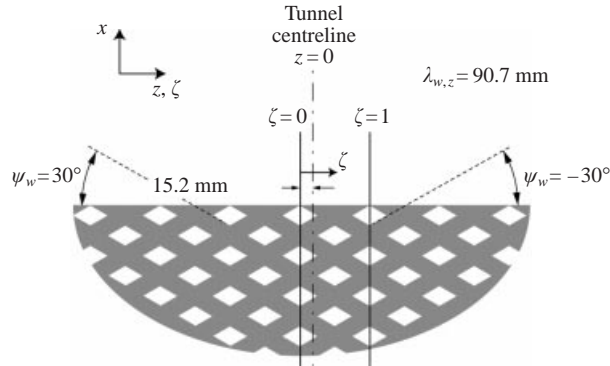
FIGURE 6. Detailed view of the surface roughness pattern and coordinate description (flow from bottom to top).
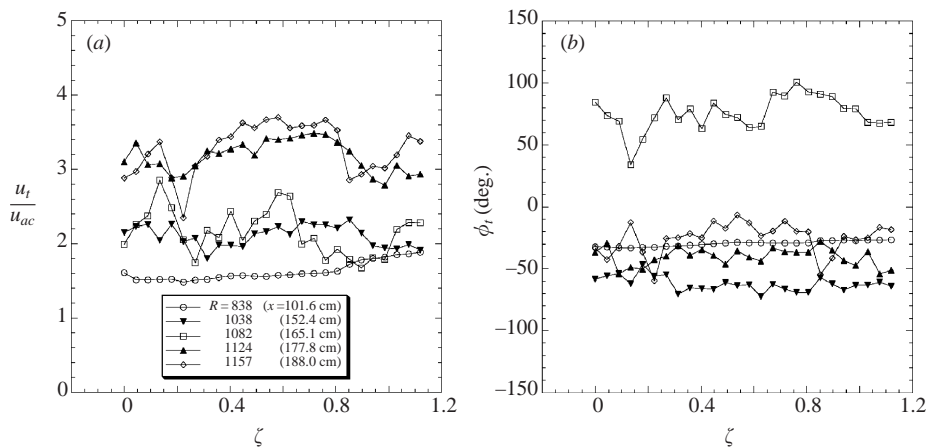

FIGURE 7. Root-mean-square narrow-band velocity at f_o, (*a*) amplitude and (*b*) phase, measured along spanwise coordinate ζ at various streamwise locations for a forcing combination of zero (ϵ_2, $\Delta h = 0$). Measurements acquired at a wall-normal location corresponding to $U/U_\infty \approx 0.40$.

the direction of x denoted in the figure. The origin of the spanwise coordinate z was taken as the tunnel centreline. Because the centrelines of the tunnel and roughness patterns did not coincide, a new normalized spanwise coordinate ζ was introduced with an offset (15.2 mm). The spanwise coordinate was defined as $\zeta = (z + 15.2)/\lambda_{w,z}$ where z is in units of mm and $\lambda_{w,z}$ is the spanwise wavelength of the roughness ($\lambda_{w,z} = 90.7$ mm). This gives a value of $\zeta = 1$ for one spanwise wavelength. Streamwise velocity measurements were acquired along the spanwise direction near the wall-normal locations corresponding to the maximum amplitude of the three-dimensional disturbance eigenfunction. The spanwise traverses typically extended approximately one spanwise wavelength of the wall roughness. Spanwise profiles of the narrow-band r.m.s. streamwise disturbance velocity, u_t, were acquired for a free-stream acoustic level of ϵ_2 on the smooth model surface, $\Delta h = 0$. These measurements were obtained to characterize the background spanwise disturbance environment, which is a function of the damping screens in the tunnel. Plots showing the spanwise distribution of u_t and ϕ_t, the disturbance phase angle, are presented in figure 7. The profiles were taken at a wall-normal location near the maximum of u_t over a streamwise distance of
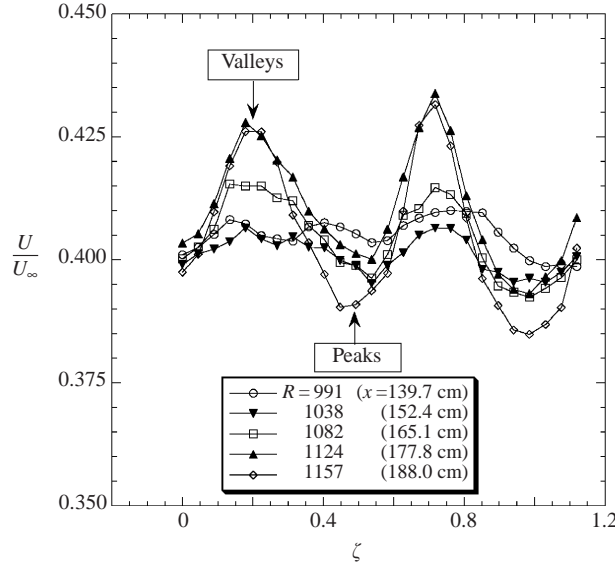
FIGURE 8. Mean streamwise velocity measured along spanwise coordinate ζ at various streamwise locations for $\epsilon_3 \Delta h_1$ and $\psi_w = \pm 30°$. Measurements were acquired at $U/U_\infty \approx 0.40$ for $\zeta = 0$ corresponding to $y/\delta \approx 0.25$ for the undisturbed profiles.

$838 < R < 1157$ ($101.6 < x < 188.0$ cm). Note that $R \approx 85.92 x_v^{1/2}$ where x_v is in cm. No significant structures in the spanwise u_t distribution were observed as is evident in part (*a*) of the figure. Similarly, spanwise variations in ϕ_t were not evident as indicated in part (*b*). The results demonstrate a relatively two-dimensional disturbance field at f_o over the limited spanwise extent of the measurements.

Results with the three-dimensional surface roughness will first be presented for a scenario where laminar-to-turbulent breakdown was not observed. The forcing combination used to obtain these results was $\epsilon_3 \Delta h_1$. Figure 8 shows a plot of mean streamwise velocity data versus the spanwise location, acquired at a wall-normal location near the maximum of u_t. The mean flow structure was very similar to the classical work of Klebanoff *et al.* (1962), although generated by a different mechanism. The location of the peaks and valleys resulting from the streaks are indicated in the figure. The peaks and valleys are defined as regions corresponding to U deficits and U surpluses, respectively. The distorted base flow resulted from the streaky structures believed to be produced by the *lift-up* effect (see Landahl 1975) of the stationary vortex system $(f/f_o, \pm \beta/\beta_w) = (0, \pm 2)$ induced by the nonlinear interaction of the primary modes $(1, \pm 1)$. The amplitude of the mean-flow distortion was seen to increase with downstream location. Data for the disturbance amplitude and phase at f_o corresponding to this configuration are presented in figure 9. The peaks and valleys are again indicated in part (*a*) of the figure. Note that the maximum u_t near $\zeta \approx 0.5$ shifts to a larger ζ value located between the peak ($\zeta \approx 0.5$) and adjacent valley ($\zeta \approx 0.8$) for $R \geqslant 1124$ ($x \geqslant 177.8$ cm). This is believed to be driven by spanwise mean-flow gradients (see the next paragraph for a discussion). The spanwise extent of the peaks was larger than that for the valleys. The valleys became narrower with downstream distance. The disturbance amplitude u_t was seen to decay for the larger R values after the initial amplification. A 180° phase shift in the disturbance phase ϕ_t was observed between adjacent peaks as seen in figure 9(*b*).
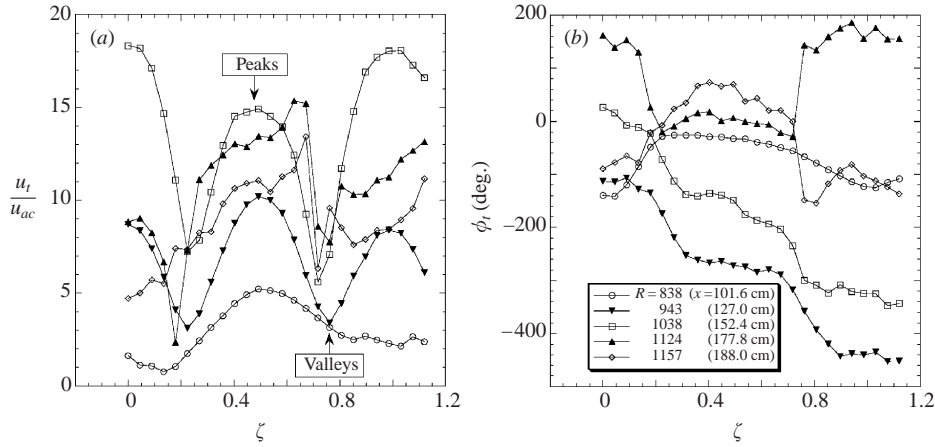
FIGURE 9. Root-mean-square narrow-band velocity at f_o, (a) amplitude and (b) phase, measured along spanwise coordinate ζ at various streamwise locations for $\epsilon_3\Delta h_1$ and $\psi_w = \pm30°$. Measurements acquired at $y/\delta \approx 0.25$ for the undisturbed profiles.
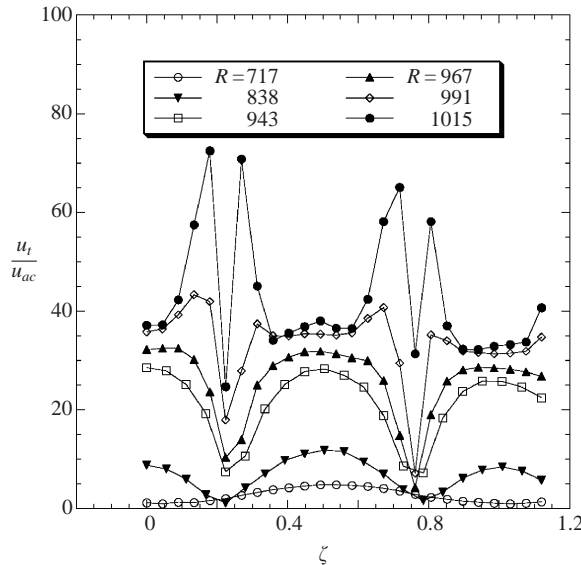

FIGURE 10. Root-mean-square narrow-band velocity at f_o measured along spanwise coordinate ζ at various streamwise locations for $\epsilon_3\Delta h_3$ and $\psi_w = \pm30°$. Measurements were acquired at $U/U_\infty \approx 0.40$ for $\zeta = 0$, which corresponds to $y/\delta \approx 0.25$–0.29 for the undisturbed profiles.

Measurements were also obtained using a larger forcing combination ($\epsilon_3\Delta h_3$) for a scenario where laminar-to-turbulent breakdown occurred. Significant three-dimensionality associated with low- and high-speed streaks was observed compared to the results in figure 8. The mean velocity (data not shown) increased by as much as 75% in the valley regions. As before for the case with $\epsilon_3\Delta h_1$, the mean flow distortions were biased to higher velocities. The corresponding narrow-band disturbance velocity amplitudes are presented in figure 10. For $R < 967$ ($x < 133.4$ cm), the spanwise distribution of u_t was largely consistent with results obtained for $\epsilon_3\Delta h_1$ (refer to figure 9a). The spanwise disturbance distribution took on a different character at $R = 991$ ($x = 139.7$ cm). An upwelling of u_t on both sides of the peaks was observed. Explosive
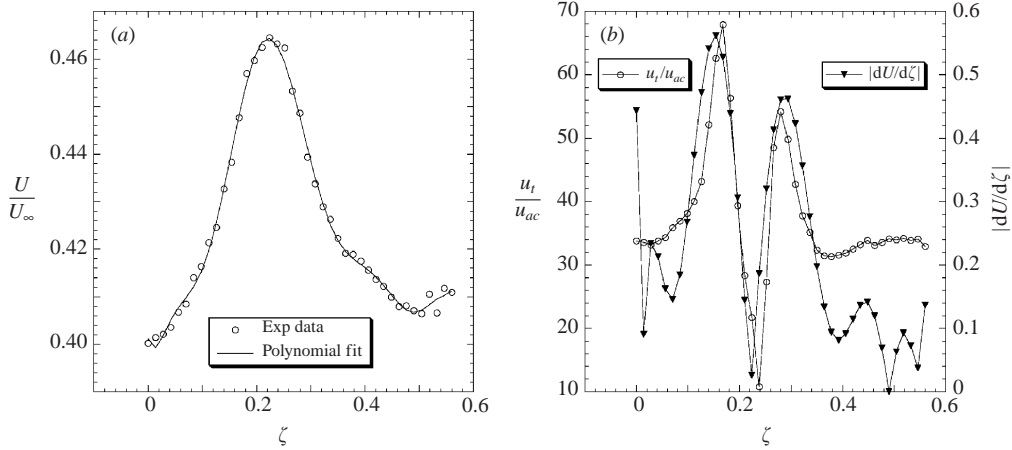
FIGURE 11. Detailed spanwise distribution of the measured (*a*) mean velocity and (*b*) r.m.s. narrow-band velocity at $R = 1015$ ($x = 146.1$ cm) for $\epsilon_3 \Delta h_3$ and $\psi_w = \pm 30°$. Curves of the polynomial regression fit to the measured data and its derivative are also included in the plots. Data obtained at $y/\delta \approx 0.26$ for the undisturbed profiles.

growths in the value of u_t at these spanwise locations were realized with streamwise distance. Velocity fluctuations as large as $u_t/U_\infty \approx 9\%$ were measured in these surveys at $R = 1082$ ($x = 165.1$ cm). Similar observations regarding the phase shift of 180° were evident in ϕ_t between adjacent peaks for this configuration relative to the configuration for $\epsilon_3 \Delta h_1$ (refer to figure 9*b*). To understand the origin of this instability, closely spaced measurements were acquired over approximately half the spanwise wavelength. Data are presented in figure 11 for $R = 1015$ ($x = 146.1$ cm). In part (*a*) of the figure, the measured mean velocity data and a corresponding polynomial regression curve fit are presented. The regression fit, which gives a good representation of the measured data except near the end points, was computed to facilitate the calculation of the mean spanwise velocity gradient $dU/d\zeta$. The spanwise distributions of the fluctuating velocity and absolute spanwise gradient are presented in figure 11(*b*). The spanwise locations of the maximum value of $|dU/d\zeta|$ coincide with the locations of large velocity fluctuations. The magnitude of u_t also scales with $|dU/d\zeta|$. This intensification of u_t appeared to be driven by the mean spanwise gradient $dU/d\zeta$. The observed intensification is believed to result from nonlinear interactions of the primary instability modes or a secondary instability. Similar finding were reported by Elofsson & Alfredsson (1998) for oblique transition in plane Poiseuille flow.

Power spectral densities at three spanwise locations are presented in figure 12 corresponding to the data presented in figure 11. The locations $\zeta = 0$ and $\zeta = 0.25$ correspond to a peak and valley, respectively; $\zeta = 0.17$ represents a location of strong spanwise mean shear. All the spectra were dominated by the energy at the forcing frequency f_o and higher harmonics. Similar harmonic cascades in the early nonlinear stages were noted in spectra observed by Breuer *et al.* (1996) and King & Breuer (2001) for two-dimensional localized and non-localized receptivity, respectively. One notable feature in the current spectra is the appearance of energy in the subharmonic frequency band not observed by King & Breuer (2001) for the laminar-to-turbulent breakdown scenario with two-dimensional roughness. More on the observed energy in the subharmonic frequency band will be provided later. For the spectra at the peak location ($\zeta = 0$), the energy bands at the fundamental and higher-harmonic frequencies are narrower than the corresponding bands for the
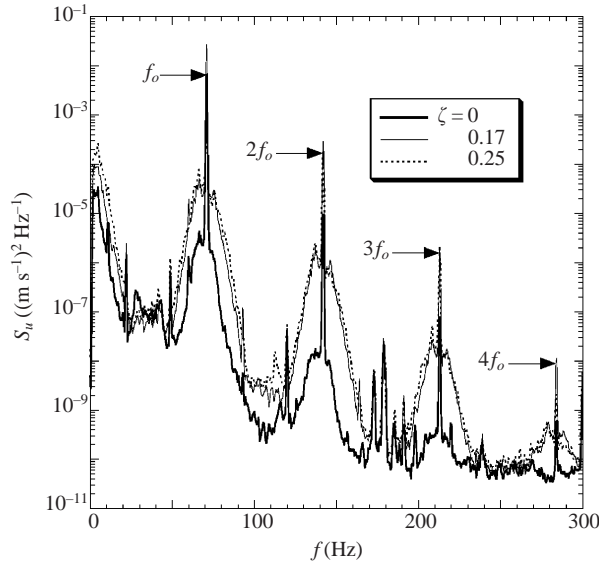
FIGURE 12. Power spectral density of the fluctuating streamwise velocity at $R = 1015$ ($x = 146.1$ cm) for three spanwise locations ($\zeta = 0$, 0.17, and 0.25). Data, corresponding to figure 11, obtained at $y/\delta \approx 0.26$ for the undisturbed profiles.

valley location. In contrast, the spectra results (not shown) obtained upstream of the observed upwelling of u_t in the spanwise profile ($R < 967$ or $x < 133.4$ cm) indicated broader energy bands at the fundamental and harmonic frequencies for peak locations. The largest broadband r.m.s. velocity u was shifted from the peak locations for x distances upstream of the upwelling in the u_t spanwise profiles to spanwise locations corresponding to maximum spanwise mean shear further downstream.

Distortion to the base flow was also examined with wall-normal measurements of the streamwise velocity field at spanwise locations corresponding to peaks and valleys. Mean velocity measurements acquired under the influence of acoustic forcing and/or wall roughness were used to compute a velocity deficit, $\delta(U/U_\infty)$, relative to the unperturbed flow (smooth surface without acoustic forcing). The velocity deficit is defined as $\delta(U/U_\infty) = U/U_\infty - U_{ref}/U_\infty$ where U and U_{ref} denote the perturbed and unperturbed (reference) velocities, respectively. The reference velocity profiles were first linearly interpolated to the wall-normal coordinate, η, of the perturbed profiles before the subtraction was performed. The U_{ref} profiles were obtained along the tunnel centreline at the desired streamwise locations (refer to profiles in figure 3). Profiles of the velocity deficit for various forcing combinations and spanwise locations are presented in figure 13. The measurements shown were all acquired at $R = 1038$ ($x = 152.4$ cm). Results on the smooth plate with no controlled forcing ($\epsilon = 0$, $\Delta h = 0$) are presented in part (*a*) of the figure for three spanwise locations over a range of approximately one spanwise wavelength. The velocity deficits were all within 1% of the U_∞. The velocity deficits in part (*b*) of the figure were obtained at a peak location ($\zeta = 0$). Measurable velocity deficits were observed for all forcing combinations, even for cases where either the acoustic forcing level, ϵ, or the roughness height, Δh, was zero. Even though the measured acoustic leading-edge receptivity coefficient was small (see King & Breuer 2001), the integrated effect of the T–S wave generated at the leading edge is measurable and produces a mean flow distortion (see (ϵ_2, 0) case in figure 13*b*), which is not evident for the smooth surface without the applied acoustic
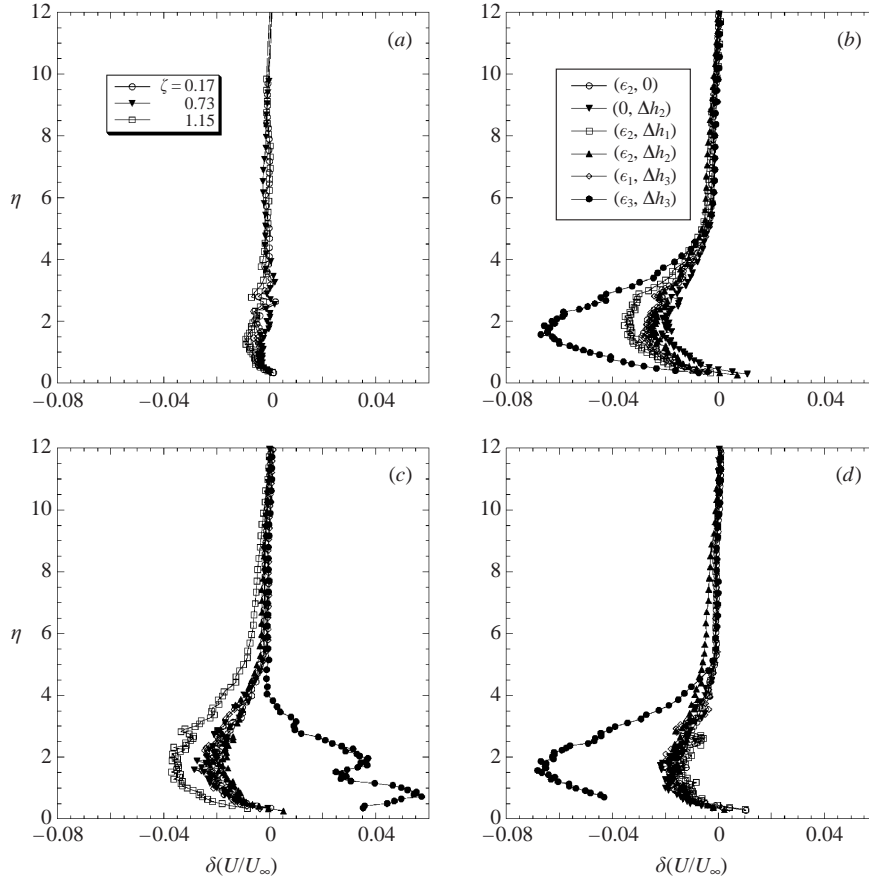
FIGURE 13. Wall-normal profiles of the velocity deficit for various forcing combinations acquired at $R = 1038$ ($x = 152.4\,\text{cm}$) and selected spanwise locations. (a) Smooth plate ($\epsilon = 0$, $\Delta h = 0$); (b) $\zeta = 0$, (c) $\zeta = 0.25$, (c) $\zeta = 0.5$; $\psi_w = \pm 30°$ (symbols are the same for b–d).

forcing (see figure 13a). This is partly due to the large two-dimensional linear growth rates compared to oblique growth rates. For the case ($\epsilon = 0$, $\Delta h = \Delta h_2$), the flow distortion is believed to result from the interaction of the background free-stream turbulence with the roughness. Velocity deficits as large as 7% of U_∞ were detected at $\eta \approx 1.7$ for the largest forcing combination ($\epsilon_3 \Delta h_3$). For forcing combinations that did not lead to breakdown, velocity deficits were typically less than 3% of U_∞. For the valley region shown in figure 13(c), velocity deficits were again observed for all forcing combinations that did not lead to breakdown. However, for the largest forcing combination that culminated in breakdown, a velocity surplus of approximately 6% was realized at a wall-normal location of $\eta \approx 0.7$. Velocity surpluses as large as 25% of U_∞ (data not shown) were measured for streamwise distances of $x = 188.0\,\text{cm}$ ($R = 1157$). The profiles in figure 13(d) correspond to another peak location at a spanwise distance of $\lambda_{w,z}/2$ from the data shown in part (b). Similar trends in the velocity deficits at the peak locations were observed as expected. The velocity-deficit profiles of the perturbed boundary layer suggest a tendency towards wall-normal inflectional velocity profiles, $U(\eta)$, except for the velocity profiles acquired in the valley regions downstream of the onset of laminar-to-turbulent breakdown.
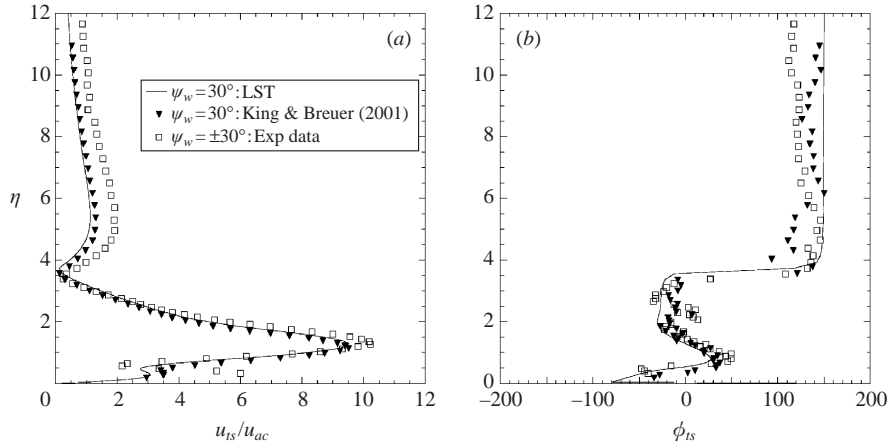
FIGURE 14. Comparison of measured eigenfunctions acquired at $R = 943$ ($x = 127.0$ cm) for ($\epsilon_z \Delta h_2$), (*a*) amplitude and (*b*) phase, for oblique and three-dimensional surface roughness (three-dimensional eigenfunction acquired along $\zeta = 0$). The computed O–S eigenfunction for the oblique wave is also shown.

3.3. *Disturbance evolution*

Three-dimensional disturbance eigenfunctions were obtained from the wall-normal measurements of the streamwise velocity. Example plots of the amplitude and phase of the measured eigenfunction are shown in figure 14 along with the measured (see King & Breuer 2001) and computed oblique O–S eigenfunction for $\psi_w = 30°$ (i.e. single oblique waviness) at $R = 943$ ($x = 127$ cm). The spanwise location of the measured three-dimensional disturbance profile ($\psi_w = \pm 30°$) was obtained at $\zeta = 0$, the centreline of the wall roughness pattern. The data presented in the figure were all obtained with the same forcing product, $\epsilon_2 \Delta h_2$. Note that the three-dimensional eigenfunction presented here represents the phase-locked velocity fluctuation at f_o for all values of the spanwise wavenumber β. The O–S and three-dimensional amplitude eigenfunctions in figure 14(*a*) show remarkable qualitative agreement. The maximum amplitude of the three-dimensional eigenfunction is approximated 15% larger than the maximum for the oblique O–S mode. This larger value of the maximum amplitude was possibly due to the contributions from other spanwise modal components. The phases of both measured eigenfunctions and LST results are in excellent agreement as depicted in figure 14(*b*). The near-wall features of the phase reversal were captured in the measurements for $\eta < 2$. The r.m.s. eigenfunction amplitudes normalized by u_{ac} and h ($= \Delta h_n / \Delta h_1$ where $n = 1$, 2 or 3) are presented in figure 15 for various values of the forcing product. The outer peak of the normalized profiles indicate a near linear response with forcing product. The same linear response was not observed for the inner peak (maximum). One plausible explanation may be related to the strength of the vertical vorticity component resulting from the distorted mean flow. The streamwise velocity contains a strong component due to the vertical vorticity. The inner peak of the eigenfunctions has been shown by Cohen *et al.* (1991) to be affected by the vertical vorticity component that is driven by the wall-normal mean shear. Since the mean shear and consequently the vertical vorticity tend to zero outside the boundary layer, the outer peaks of the eigenfunctions are not significantly influenced by the vertical vorticity component.

Wave kinematics were computed using closely spaced velocity data measured over a streamwise distance of approximately $1.5\lambda_{w,x}$. Measurements were acquired
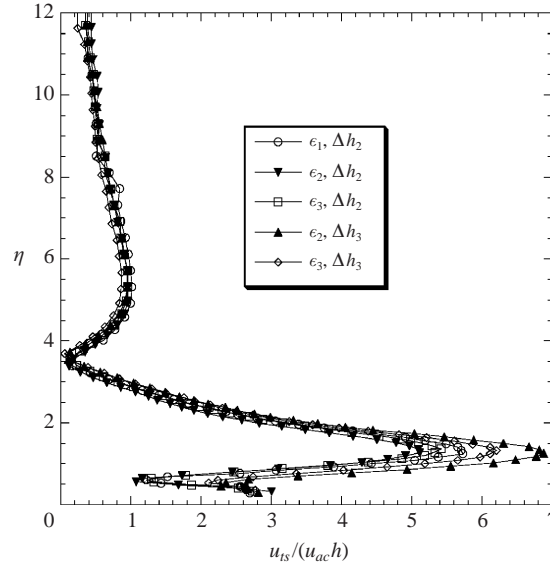
FIGURE 15. Normalized three-dimensional disturbance amplitudes acquired at $R = 943$ ($x = 127.0$ cm) for $\psi_w = \pm 30°$ for various values of u_{ac} and Δh. Measurements taken along $\zeta = 0$.

at $\zeta = 0$ (peak) and $\zeta = 0.25$ (valley) at a fixed wall-normal location near the maximum amplitude of the three-dimensional eigenfunction. The disturbance phase speeds measured were in the range of $0.34 < c_{ph}/U_\infty < 0.37$ ($\bar{c}_{ph}/U_\infty = 0.35$) at a streamwise location corresponding to $R \approx 1038$ for all possible forcing combinations. The wall-normal location of the critical layer ($\eta \approx 1$) was just below the location corresponding to the maximum amplitude of the three-dimensional eigenfunction ($\eta \approx 1.2$). Phase speed results are consistent with those measured for an oblique O–S mode by King & Breuer (2001).

As a measure of the streak amplitude, ΔU was defined as the difference between the maximum (valley location) and minimum (peak location) value of U in the spanwise profile at a given streamwise and wall-normal location. A plot of the streak amplitude versus streamwise distance is presented in figure 16 for two forcing combinations, $\epsilon_3 \Delta h_1$ and $\epsilon_3 \Delta h_3$. The spanwise U measurements were obtained at wall-normal locations near the maximum eigenfunction amplitude at f_o. Streak amplification was observed for both scenarios for large downstream distances. For the configuration where the flow remained laminar ($\epsilon_3 \Delta h_1$), ΔU remained relatively constant over the range $838 < R < 1038$ ($101.6 < x < 152.4$ cm) and streak amplification was observed further downstream ($R > 1038$). For the largest forcing product where nonlinear breakdown occurred, streak amplification was observed for all measurements. The growth rate was seen to increase at $R = 967$ ($x = 133.4$ cm) near the first occurrence of the upwelling of u_t on the sides of peaks in the spanwise profiles. The growth rate then decreased further downstream at $R = 1038$ ($x = 152.4$ cm). It is interesting to note that the streak amplitudes measured at the first streamwise position ($R = 838$ or $x = 101.6$ cm), which was approximately 21 cm downstream of the trailing edge of the roughness samples, were the same for both forcing combinations (factor of 4 difference in $\epsilon \Delta h$). Since the stationary streamwise vortex system $(0, \pm 2)$ was responsible for the formation of the streaks, this suggests that the streamwise vortex systems produced by the nonlinear interaction of the primary modes $(1, \pm 1)$ were of equal
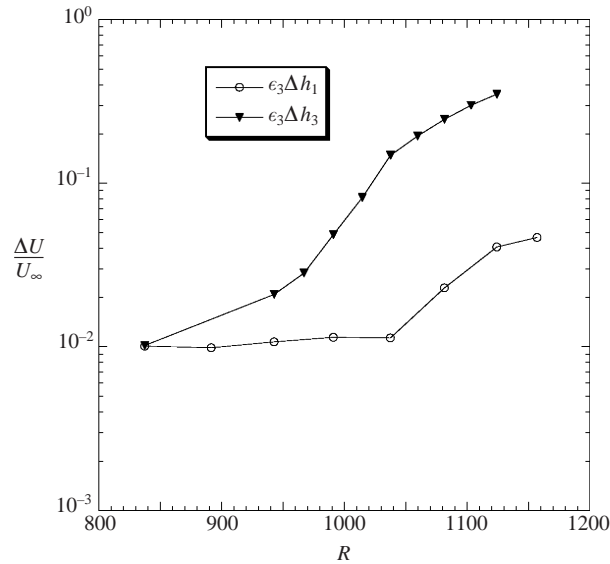
FIGURE 16. Streamwise distribution of the measured streak amplitude, ΔU, at the indicated forcing combinations. Measurements were acquired at wall-normal locations corresponding to $U/U_\infty \approx 0.40$ at $\zeta = 0$.

strengths for both forcing combinations. The equal strengths of the vortex systems at $R = 838$ may imply that the initial nonlinear interaction reached a saturated state by $R = 838$ (sufficient data are not available for upstream locations). This leads one to postulate that the significant difference observed in the streak amplification rates for $R > 838$ was primarily due to nonlinear interactions of non-stationary boundary-layer disturbances assuming some threshold amplitude of the $(0, \pm 2)$ mode was satisfied.

It was instructive to examine the disturbance evolution in the frequency–wavenumber plane. This was done by conducting spanwise surveys of the streamwise velocity at wall-normal locations near the maximum eigenfunction amplitude at f_o for several x-locations. The spanwise surveys extended 101.6 mm ($0 < \zeta < 1.12$) with a spacing of either 4.1 mm or 5.1 mm. Temporal Fourier transforms of the velocity were computed at each data point and the energy in a 2 Hz bandwidth about the desired frequencies ($f_o, 2f_o, 3f_o, \ldots$) was computed. Spanwise energy profiles were then constructed for each desired frequency using the energy computed from the temporal spectra and the corresponding spanwise locations. Spatial Fourier transforms were then applied to the spanwise energy profiles to obtain the modal components of the velocity, $u_t(f, \beta)$. Figure 17 presents results obtained for the forcing combinations discussed above. Modal velocities are presented for (i) the primary oblique modes $(1, 1)$, (ii) the first set of nonlinear interactions $(0, 0)$, $(0, 2)$, $(2, 0)$ and $(2, 2)$, and (iii) selected higher-order interactions $(1, 3)$, $(3, 1)$ and $(3, 3)$. Note that the $\pm$ on the span-wise wavenumber component was dropped. For the configuration where the flow remained laminar ($\epsilon_3 \Delta h_1$), the modal data in figure 17(a) indicate a dampening of all the significant non-stationary modes after some initial amplification. However, when laminar-to-turbulent breakdown was present ($\epsilon_3 \Delta h_3$), all non-stationary modes were seen to amplify significantly as expected (see figure 17b). Excellent qualitative agreement between the measured modal velocities in figure 17 and the simulation results of Joslin *et al.* (1993) was observed as described below. For the simulation where the flow remained laminar, all non-stationary modes were first amplified and then dampened.
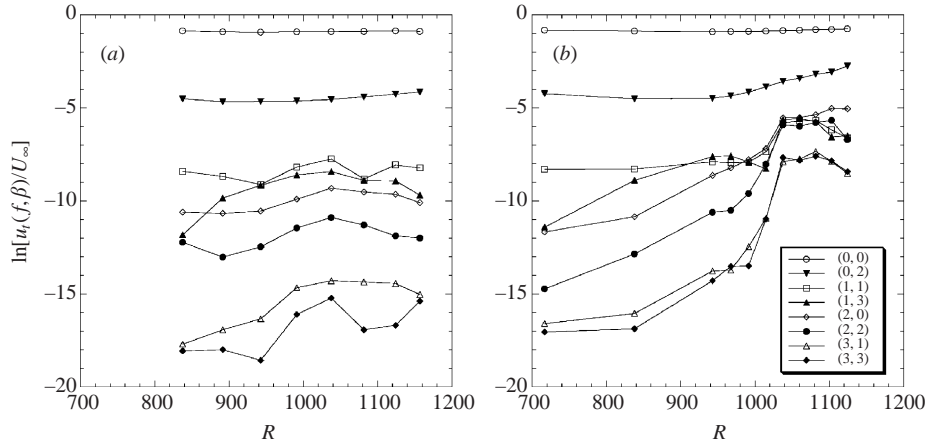
FIGURE 17. Modal velocity distribution of the measured streamwise velocity for (*a*) $\epsilon_3 \Delta h_1$ and (*b*) $\epsilon_3 \Delta h_3$ and $\psi_w = \pm 30°$. The mode designations given in the plot legends are $(f/f_o, \beta/\beta_w)$. Spanwise measurements acquired at wall-normal locations corresponding to $U/U_\infty \approx 0.40$ at $\zeta = 0$.

The streamwise vortex mode $(0, 2)$ was seen to have an initial amplification significantly larger than the other modes due to the self-interaction of the primary modes $(1, 1)$ in the simulation. The fact that the current experimental disturbance input did not contain a $(0, 2)$ mode implies that the same was true for the current results in that the $(0, 2)$ mode was more than an order of magnitude larger than any other non-stationary mode. The $(1, 3)$ mode, which resulted from a nonlinear interaction of the $(0, 2)$ and $(1, 1)$ modes, was seen to overtake the first set of excited modes, namely the $(2, 0)$ and $(2, 2)$ modes, in both the simulation and experiment. For the simulation results with breakdown, the $(0, 2)$ mode is again the dominant higher-order mode as in the experimental results. The non-stationary modes now grow with significantly larger growth rates than the case where the flow remained laminar.

For comparison, the modal velocity data for the $(1, 1)$, $(0, 2)$ and $(1, 3)$ modes are presented in figure 18 for both forcing combinations. The open symbols represent data for $\epsilon_3 \Delta h_1$ and closed symbols for $\epsilon_3 \Delta h_3$. The relative amplitudes between the corresponding modes are clearly illustrated in the figure. The primary oblique $(1, 1)$ mode at $R = 838$ for both forcing products was approximately equal, indicating that the $(1, 1)$ modes may be in a saturated state. The modal velocity corresponding to the $(0, 2)$ mode has a similar amplification curve as the streak amplitude ΔU presented earlier (see figure 16). The modal data also support the conclusion drawn earlier that the $(0, 2)$ modes at $R = 838$ were of equal strength despite the difference in the initial forcing amplitudes, indicating a saturated $(0, 2)$ mode at $R = 838$. However, the same was not true for the non-stationary $(1, 3)$ mode at $R = 838$. For the larger forcing amplitude, the $(1, 3)$ mode is expected to have a larger initial amplitude due to the nonlinear interaction of the $(1, 1)$ and $(0, 2)$ modes followed by a subsequent growth due to a linear mechanism. This is clearly illustrated in the figure where the modal $(1, 3)$ velocity for the largest forcing combination was approximately a factor of 20 larger than that for $\epsilon_3 \Delta h_1$. It is plausible that after some critical amplitude of the $(1, 3)$ mode was reached, a nonlinear (feedback) interaction of the $(1, 1)$ mode with the $(1, 3)$ mode was responsible for the enhancement of the stationary $(0, 2)$ mode. These results support the conjecture proposed earlier concerning the observed differences in the growth rates of the measured streak amplitudes with the forcing-combination
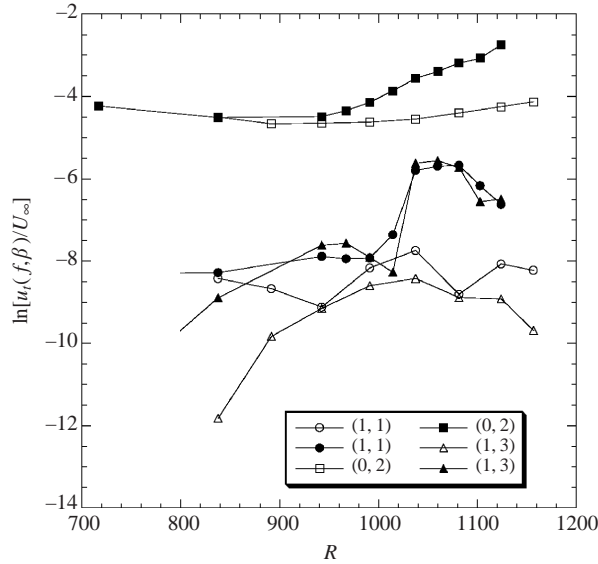
FIGURE 18. Comparison of the measured modal velocity distributions for the $(1,1)$, $(1,3)$, and $(0,2)$ modes. Data taken from figure 17 for $\epsilon_3\Delta h_1$ (open symbols) and $\epsilon_3\Delta h_3$ (solid symbols).

amplitude. The energy transfer between modes appears to favour the low frequencies as depicted in the modal velocity data in figure 17 and other data not shown. Similar findings, the so-called 'β-cascade', have been reported in the simulations of Henningson, Lundbladh & Johansson (1993) and the experiment of Breuer *et al.* (1997) for localized disturbances in plane Poiseuille flow and boundary-layer flow, respectively.

Wall-normal surveys of the streamwise velocity at several streamwise locations were acquired at two spanwise locations corresponding to a peak and valley for various levels of $\epsilon\Delta h$. The maximum amplitude of the measured eigenfunction profiles (inclusive of all spanwise wavenumbers present at f_o) were plotted versus the streamwise location. The normalized amplification curves (w.r.t. u_{ac} and h) for the various forcing combinations at the peak location ($\zeta = 0$) do not collapse. Again, this may be a result of contributions from other spanwise modal components and/or the effects of vertical vorticity on u_{ts}. Transition occurred in the valley region ($\zeta = 0.25$) before it occurred in the peak region ($\zeta = 0$). A plot of u/U_∞ versus Reynolds number for a wall-normal location of $\eta \approx 1.2$ is given in figure 19. The transition Reynolds number is in the approximate range of $9.6 \times 10^5 < Re_{tr} < 1.2 \times 10^6$.

Broadband spectra for r.m.s. velocity data at a valley location are presented in figure 20 for a forcing combination ($\epsilon_2\Delta h_2$) that did not result in breakdown. The spectral content at a peak location ($\zeta = 0$) was not very different from that at a valley location ($\zeta = 0.25$). Wave amplification was observed in the unstable T–S band at both spanwise locations. Figure 21 shows broadband spectra for the largest forcing product at a peak and valley spanwise location. At the peak location shown in part (*a*) of the figure, energy concentrated in frequency bands about the fundamental and first two harmonics is clearly evident in the transitional zone. The spectra indicate an abrupt change in the flow state from laminar to turbulent. At the valley in part (*b*) of the figure, energy bands at the fundamental and higher-harmonics frequencies (up to the low-pass filter settings) dominated the spectrum in the transitional zone. Recall that similar spectral behaviour was observed by Breuer *et al.* (1996) and
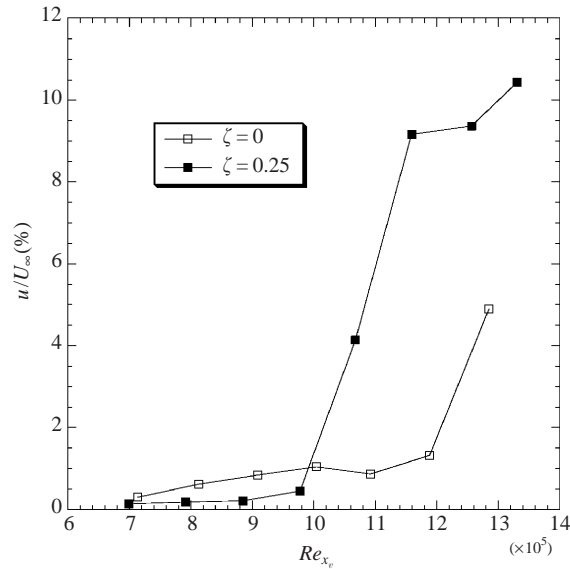
FIGURE 19. u/U_∞ versus Reynolds number for a wall-normal location of $\eta \approx 1.2$ at a peak ($\zeta = 0$) and valley ($\zeta = 0.25$) location for $\epsilon_3, \Delta h_3$ and $\psi_w = \pm 30°$.
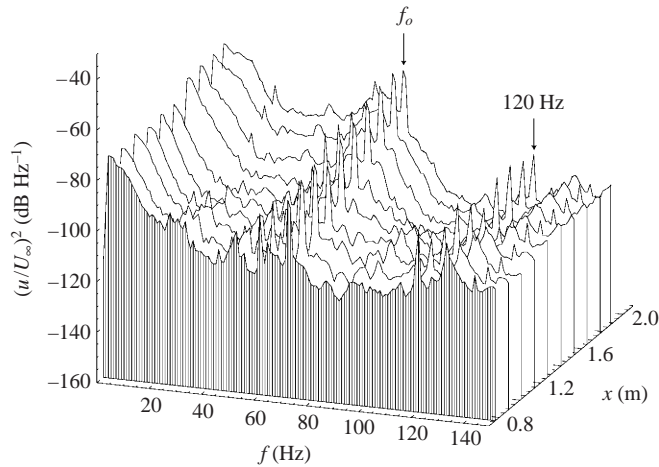

FIGURE 20. Spectra of streamwise velocity taken at a valley location $\zeta = 0.25$ and $u_{t,max}$ ($U/U_\infty \approx 0.40$) for a scenario where breakdown did not occur ($\epsilon_2 \Delta h_2$). Electronic noise at $f = 120$ Hz is noted.

King & Breuer (2001) with initial two-dimensional disturbance inputs. The measured streamwise location at which the harmonic bands first became dominant ($R = 1038$, $x = 152.4$ cm) was just downstream of the appearance of the upwelling of $u_t(f_o)$ in the spanwise profiles resulting from the strong spanwise mean shear. The transitional region associated with the valley appeared to be dominated by coherent disturbances and to be more gradual than at the peak location.

For the flow configuration where breakdown occurred with two-dimensional wall waviness (see King & Breuer 2001), energy at subharmonic frequencies was not observed. To focus on the energy in the subharmonic frequency range, the spectral data in figure 21 were re-plotted to magnify the desired frequency range. The resulting
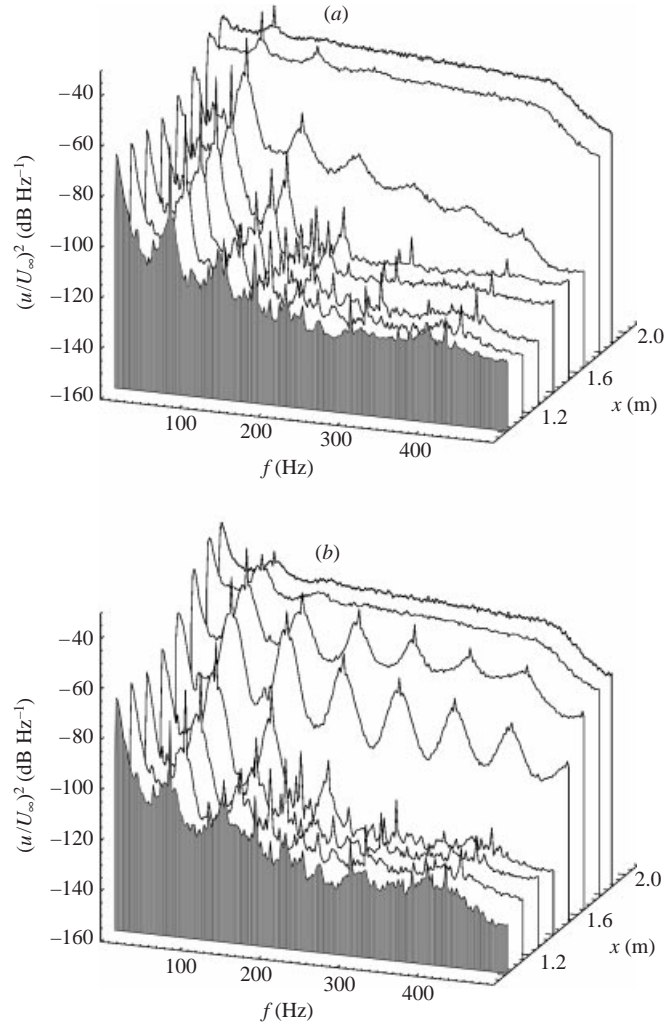
FIGURE 21. Spectra of streamwise velocity taken at $u_{t,max}$ ($U/U_\infty \approx 0.40$) for a scenario where breakdown occurred ($\epsilon_3 \Delta h_3$). Measurements were obtained along spanwise locations corresponding to (a) a peak $\zeta = 0$ and (b) a valley $\zeta = 0.25$.

spectra in addition to the spectra acquired with two-dimensional wall waviness (shown for comparison) are presented in figure 22 for $\epsilon_3 \Delta h_3$. Energy in the subharmonic frequency band was evident in the spectra for the three-dimensional wall roughness. The energy in the subharmonic band was not dominated by the actual subharmonic frequency ($f_o/2 = 35.5$ Hz) but by a broad band of frequencies ($20 < f < 50$ Hz). The subharmonic energy at the peak location ($\zeta = 0$) was found to be more significant than the associated energy at the valley location (refer to parts (b) and (c) of the figure). At the peak location, narrow-band energy centred at $f = 22$ Hz and 48 Hz, for which the source of either was unknown, was evident. Either one of these disturbance energies can possibly interact with the fundamental frequency ($f_o = 71$ Hz) to produce the other. Higher-order spectral methods applied to multipoint measurements are necessary to resolve the issue of a sum or difference interaction. Such measurements were not acquired in this study. Broader energy bands were also observed for central
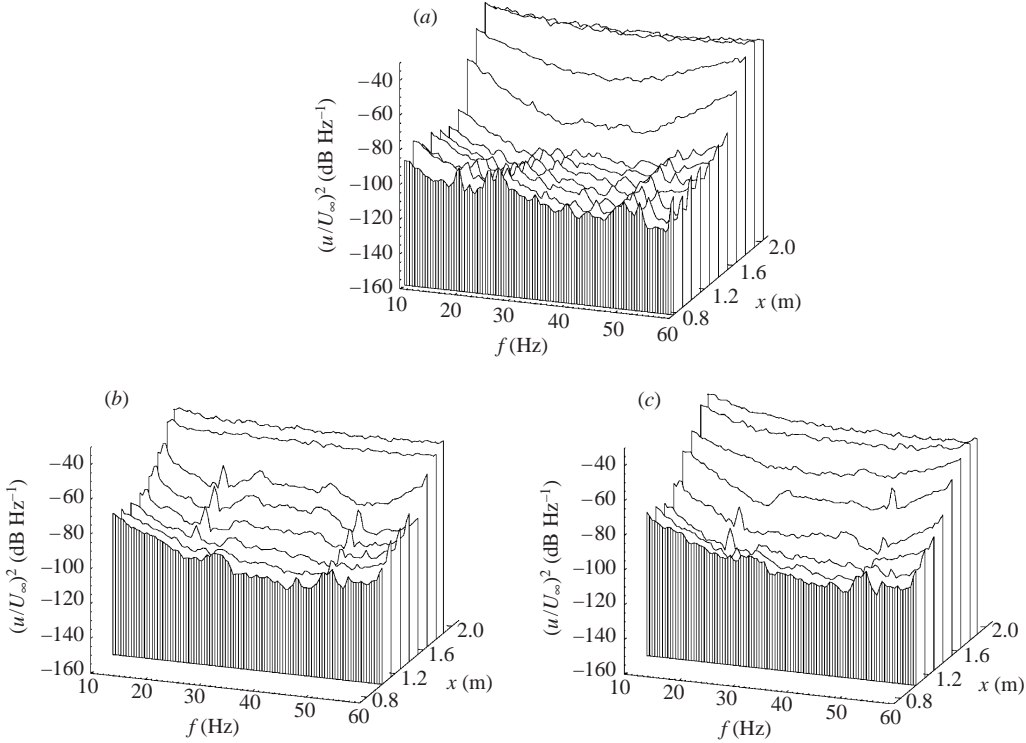
FIGURE 22. Spectra of streamwise velocity in the subharmonic frequency range taken at $u_{t,max}$ for scenarios where breakdown occurred. Measurements are shown over a range of streamwise locations for (*a*) two-dimensional surface waviness, (*b*) three-dimensional roughness along $\zeta = 0$, and (*c*) three-dimensional roughness along $\zeta = 0.25$.

frequencies of $f = 29\,\mathrm{Hz}$ and $42\,\mathrm{Hz}$. The same applies to this frequency pair as to $f = 22\,\mathrm{Hz}$ and $48\,\mathrm{Hz}$. The first of the main points to be made here is the evidence of energy in the subharmonic frequency range, though much less than the energy in the harmonic frequency bands. Secondly, at the peak location where the subharmonic energy band was largest, more spectral filling/broadening at frequencies in between the harmonic bands was observed in the transitioning boundary layer (see figure 21) implying nonlinear interactions between subharmonic and harmonic disturbances. Last but not least, despite the presence of subharmonic energy, the dominant energy transfer is clearly to the higher harmonics as is evident from the spectra shown in figure 21. In other words, there is some redistribution of energy (second-order effect) to the subharmonic frequency band but the physical process responsible for spectral broadening is dominated by the nonlinear interactions (self and mutual) of the fundamental and higher-harmonic energies.

4. Concluding remarks

It has long been recognized that the occurrence of three-dimensional disturbances is necessary for the laminar-to-turbulent transition process in wall-bounded flows. The selection process of boundary layers in the so-called *natural* transition has suggested oblique modes as an essential ingredient for the onset of breakdown. For this reason, boundary-layer transition was experimentally forced by exciting a pair of oppositely

oriented oblique O–S modes, $(f/f_o, \pm\beta/\beta_w) = (1, \pm1)$, and investigated to identify the controlling physics of the transition process. This non-canonical transition scenario bypasses the traditional two-dimensional T–S disturbances and utilizes the oppositely oriented oblique O–S disturbances as primary modes.

Previous investigations of this nature by Elofsson & Alfredsson (1998, 2000) and Wiegel (1996) have used vibrating ribbons, or periodic surface blowing/suction to generate the flow disturbances. In this study, a clean pair of oppositely oriented oblique modes was introduced in a laminar boundary layer utilizing the approach of King & Breuer (2001): the acoustic receptivity of the boundary layer to surface roughness. The technique used has some features that are worth highlighting. First, the time scales and the spatial scales are completely decoupled – the first being provided by the acoustic field and the second coming from the surface roughness pattern. This makes the experiment very clean and removes difficulties often encountered with non-uniform ribbon excitation or difficulties in generating uniform or finely controlled surface pressure oscillations. Secondly, the forcing is very amenable to simulation in either theoretical or numerical models and for this reason, detailed comparisons between theory, numerics and experiment should be possible. This study also provides a useful link between well-documented initial conditions and the occurrence, or non-occurrence, of transition.

The oblique primary modes, $(f/f_o, \pm\beta/\beta_w) = (1, \pm1)$, were observed to interact nonlinearly to create low- and high-speed streaks that culminated in a peak–valley structure of the spanwise U-profiles. The growth rates of the streaky structures were believed to be enhanced by nonlinear (feedback) interactions of two non-stationary boundary-layer disturbance modes, namely the $(1, 1)$ mode and $(1, 3)$ mode. An intensification of u_t in regions with large spanwise velocity gradients, $|dU/d\zeta|$, was observed that ultimately lead to laminar-to-turbulent transition. Measured modal velocities were in excellent qualitative agreement with results obtained from spatial direct numerical simulation by Joslin *et al.* (1993). The energy transfer between the measured modes appeared to favour low frequencies, the so-called β-cascade as noted by Henningson *et al.* (1993) and later by Breuer *et al.* (1997). In the laminar-to-turbulent transition region, the velocity spectra were dominated by the energy at the forcing frequency f_o and higher harmonics, i.e. similar to harmonic cascades observed by Breuer *et al.* (1996) and King & Breuer (2001) for two-dimensional primary disturbances. Energy in the subharmonic frequency range was also observed in the spectra, though much less than the energy in the harmonic frequency bands. More spectral filling/broadening at frequencies in between the harmonic bands was observed in the transitioning boundary layer than observed by King & Breuer (2001) for two-dimensional primary disturbances, implying nonlinear interactions between subharmonic and harmonic disturbances. The results demonstrate some redistribution of energy (second-order effect) to the subharmonic frequency band but the physical process responsible for spectral broadening is dominated by the nonlinear interactions (self and mutual) of the fundamental and higher-harmonic energies as found with fundamental (K-type) breakdown.

REFERENCES

BAKCHINOV, A. A., GREK, G. R., KLINGMANN, B. G. B. & KOZLOV, V. V. 1995 Transition experiments in a boundary layer with embedded streamwise vortices. *Phys. Fluids* **7**, 820–832.

BERLIN, S., LUNDBLADH, A. & HENNINGSON, D. S. 1994 Spatial simulations of oblique transition in a boundary layer, *Phys. Fluids* A **6**, 1949–1951.

BERLIN, S., WIEGEL, M. & HENNINGSON, D. S. 1999 Numerical and experimental investigations of oblique boundary layer transition. *J. Fluid Mech.* **393**, 23–57.

BREUER, K. S., COHEN, J. & HARITONIDIS, J. H. 1997 The late stages of transition induced by a low-amplitude wavepacket in a laminar boundary layer. *J. Fluid Mech.* **340**, 395–411.

BREUER, K. S., DZENITIS, E. G., GUNNARSSON, J. & ULLMAR, M. 1996 Linear and nonlinear evolution of boundary layer instabilities generated by acoustic-receptivity mechanisms. *Phys. Fluids* **8**, 1415–1423.

COHEN, J., BREUER, K. S. & HARITONIDIS, J. H. 1991 On the evolution of a wave packet in a laminar boundary layer, *J. Fluid Mech.* **225**, 575–606.

CORKE, T. C. & MANGANO, R. A. 1989 Resonant growth of three-dimensional modes in transitioning Blasius boundary layers. *J. Fluid Mech.* **209**, 93–150.

CRAIK, A. D. D. 1971 Non-linear resonant instability in boundary layers. *J. Fluid Mech.* **50**, 393–413.

ELOFSSON, P. A. & ALFREDSSON, P. H. 1998 An experimental study of oblique transition in plane Poiseuille flow. *J. Fluid Mech.* **358**, 177–202.

ELOFSSON, P. A. & ALFREDSSON, P. H. 2000 An experimental study of oblique transition in a Blasius boundary layer flow. *Eur. J. Mech.* B/*Fluids* **19**, 615–636.

ELOFSSON, P. A., KAWAKAMI, M. & ALFREDSSON, P. H. 1999 Experiments on the stability of streamwise streaks in plane Poiseuille flow. *Phys. Fluids* **11**, 915–930.

GASTER, M. & GRANT, I. 1975 An experimental investigation of the formation and development of a wave packet in a laminar boundary layer. *Proc. R. Soc. Lond.* A **347**, 253–269.

HENNINGSON, D. S., LUNDBLADH, A. & JOHANSSON, A. V. 1993 A mechanism for bypass transition from localized disturbances in wall-bounded shear flows *J. Fluid Mech.* **250**, 169–207.

HERBERT, T. 1985 Three-dimensional phenomena in the transitional flat-plate boundary layer. *AIAA Paper* 85-0489.

HERBERT, T. 1988 Secondary Instability of boundary layers. *Annu. Rev. Fluid Mech.* **20**, 487–526.

JOSLIN, R. D., STREETT, C. L. & CHANG, C.-L. 1993 Spatial direct numerical simulation of boundary-layer transition mechanisms: Validation of PSE theory. *Theoret. Comput. Fluid Dyn.* **4**, 271–288.

KACHANOV, Y. S., KOZLOV V. V. & LEVCHENKO, V. Y. 1977 Nonlinear development of a wave in a boundary layer. *Fluid Dyn.* **12**, 383–390.

KACHANOV, Y. S. & LEVCHENKO, V. Y. 1984 The resonant interaction of disturbances at laminar-turbulent transition in a boundary layer. *J. Fluid Mech.* **138**, 209–247.

KING, R. A. 2000 Receptivity and growth of two- and three-dimensional disturbances in a Blasius boundary layer. PhD thesis, Massachusetts Institute of Technology, Cambridge, MA.

KING, R. A. & BREUER, K. S. 2001 Acoustic receptivity and evolution of two-dimensional and oblique disturbances in a Blasius boundary layer. *J. Fluid Mech.* **432**, 69–90.

KLEBANOFF, P. S. & TIDSTROM, K. D. 1959 Evolution of amplified waves leading to transition in a boundary layer with zero pressure gradient. *NASA TN* D-195.

KLEBANOFF, P. S., TIDSTROM, K. D. & SARGENT, L. M. 1962 The three-dimensional nature of boundary-layer instability. *J. Fluid Mech.* **12**, 1–34.

KNAPP, C. F. & ROACHE, P. J. 1968 A combined visual and hot-wire anemometer investigation of boundary-layer transition. *AIAA J.* **6**, 29–36.

LANDAHL, M. T. 1975 Wave breakdown and turbulence. *SIAM J. Appl. Maths* **28**, 735–756.

LANDAHL, M. T. 1980 A note on an algebraic instability of inviscid parallel shear flows. *J. Fluid Mech.* **98**, 243–251.

MORKOVIN, M. V. 1969 On the many faces of transition. In *Viscous Drag Reduction*, (ed. C. S. Wells), pp. 1–31. Plenum.

SARIC, W. S., KOZLOV, V. V. & LEVCHENKO, V. Y. 1984 Forced and unforced subharmonic resonance in boundary-layer transition. *AIAA Paper* 84-0007.

SARIC, W. S. & THOMAS, A. S. W. 1984 Experiments on the subharmonic route to turbulence in boundary layers. In *Turbulence and Chaotic Phenomena in Fluids* (ed. T. Tatsumi), pp. 117–122. North-Holland: Elsevier.

SCHMID, P. J. & HENNINGSON, D. S. 1992 A new mechanism for rapid transition involving a pair of oblique waves. *Phys. Fluids* A **4**, 1986–1989.

WIEGEL, M. 1996 Experimentelle Untersuchung von kontrolliert angeregten dreidimensionalen Wellen in einer Blasius-Grenzschicht. PhD thesis, Der Fakultät für Maschinenwesen der Universität Hannover, Hannover, Germany.

WIEGEL, M. & FISCHER, M. 1995 Utilizing a laser light sheet technique in a boundary-layer flow to study different transition types. In *Flow Visualization VII* (ed. J. P. Crowder), pp. 432–437. Begell House.